

Experimentally Determined Optical Properties of a Polydisperse Carbon Black Cloud for a Solar Particle Receiver

Rudi Bertocchi
Abraham Kribus*
Jacob Karni

Environmental Sciences and
Energy Research Dept.,
Weizmann Institute of Science,
Rehovot 76100, Israel

Measured physical and optical properties of a stable polydisperse carbon black particle cloud at 532 nm and 1064 nm are reported. The particle cloud consisted of 99.7% spheroid primary particles (45–570 nm diameter) and 0.3% large irregularly shaped agglomerates (1.2–7.25 μm equivalent diameter). Although the numerical fraction of the agglomerates was only 0.2%, they contributed 60% to the cloud's scattering cross section. The extinction coefficient, scattering coefficient and the scattering phase function were measured for both parallel and perpendicular polarized radiation at linear extinction coefficients ranging from 0.6 to 4.1 m^{-1} . The cloud exhibited strong forward scattering, with 62% of all scattered energy in a forward lobe of 15° at 532 nm and 48% at 1064 nm. The scattering albedo was measured to 35% at 532 nm and 47% at 1064 nm. The dimensionless extinction coefficient was measured to 8.25 at 532 nm. The experimental data was compared to standard Mie theory by integrating the weighed contribution based on particle size, including agglomerates, according to the detailed measured population distribution. Neglecting the contribution of the agglomerates to the cloud's optical properties was shown to introduce discrepancies between Mie theory and measured results. The results indicate that the-Mie theory can be used for estimating the optical properties of a partially agglomerated carbon black particle cloud for simulation of a solar particle receiver. [DOI: 10.1115/1.1756924]

Keywords: Optical Properties, Scattering Phase Function, Radiative Transfer Equation, Mie Theory, Carbon Particles

1 Introduction

A solar receiver with a working gas containing suspended radiation absorbing particles can reach very high temperatures, compared to more conventional receivers where the radiation is absorbed in a stationary solid element and then transferred to the gas by convection. Such a solar particle receiver operates by seeding the process gas with a large numerical amount of small carbon black particles. The suspension is irradiated by concentrated solar radiation. The incident radiation energy is absorbed by the carbon particles and then transferred to the gas by molecular actions. The concept of using a suspended carbon particle cloud within a transparent gas was first reported in 1979 by Abdelrahman [1] and Hunt [2]. Hunt & Brown [3] first demonstrated this concept, using a particle receiver to heat air up to 1000 K. Recently, Bertocchi et al. [4] developed a different design of a particle receiver that has successfully heated a nitrogen gas stream up to 2120 K. A different type of particle receiver, where the particles are heated in order to perform a chemical reaction, was extensively investigated by Steinfeld et al. [5,6].

The motivation behind the work presented in this paper is to improve the understanding of the energy transport in a high temperature solar particle receiver. Detailed knowledge of the carbon particle suspension's optical properties is essential for understanding and predicting the radiative energy transport in the mixture, directly affecting the design of the solar particle receiver. The interaction of small carbon particles dispersed in a gas with radia-

tion is of interest in additional disciplines as: combustion [7], atmospheric transport of aerosols [8] and pollution emissions [9]. Previous studies of carbon particles have focused on soot particles generated in flames [7]. These soot clouds are dominated by agglomerates, each consisting of a large number of small primary particles arranged in complex fractal shapes. In the solar particle receiver case, a cloud consisting of a homogeneous particle size is desirable. Such a cloud can be generated by dispersing carbon powder in a carrying gas rather than *in-situ* pyrolysis of a hydrocarbon [10]. The current work addresses the radiative interaction of particle clouds generated by the dispersion method and consisting of both primary particles and agglomerates.

The optical properties of small primary particles are well represented by the general Mie theory [11]. The application of Mie theory weighed by an assumed or measured particle size distributions may yield a reasonable prediction of the properties of a polydisperse cloud composed of simple primary particles [12–14]. However, the problem of agglomerated clouds is considerably more difficult due to the geometric complexity of the agglomerates and their large contribution to the optical properties. It is essential to account for the agglomerates contribution to the optical properties, even for numerical agglomeration fractions less than 0.5%, in order to obtain reasonable results from Mie theory applied to partially agglomerated particle clouds. In the current study, the experimental results were compared to predictions made using Mie theory based on the measured particle size distribution, which provided weights for the contributions of different particles sizes to the optical properties. The agreement between Mie theory and the measurements was satisfactory when the effect of the agglomerates was accounted for.

*Present address: School of Mechanical Engineering, Faculty of Engineering, Tel Aviv University, Tel Aviv 69978, Israel.

Contributed by the Solar Energy Division of THE AMERICAN SOCIETY OF MECHANICAL ENGINEERS for publication in the ASME JOURNAL OF SOLAR ENERGY ENGINEERING. Manuscript received by the ASME Solar Division September 2003; final revision March 2004. Associate Editor: A. Kribus.

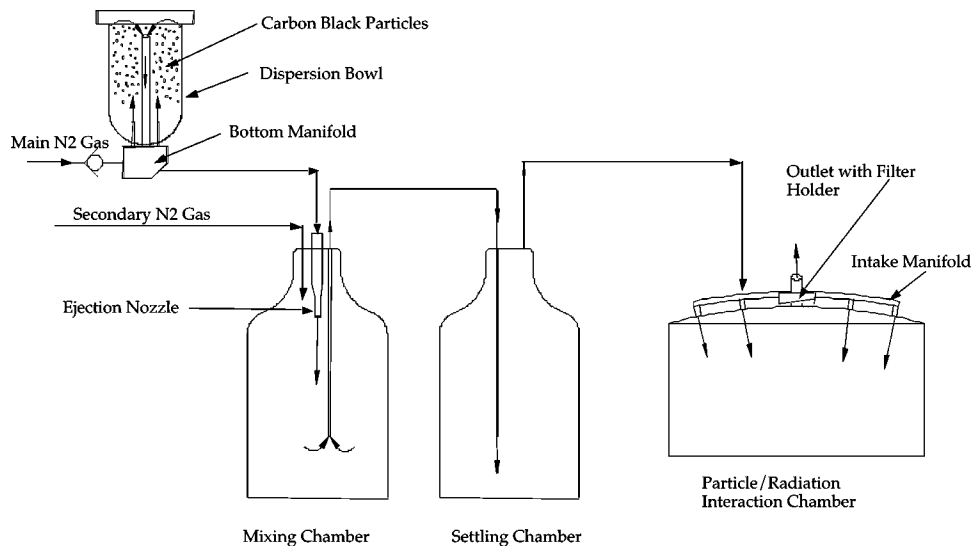


Fig. 1 Schematic of Apparatus for Particle Cloud Generation System

2 Experimental Apparatus and Procedure

A stable particle cloud was generated by dispersing dried carbon black powder into a carrying gas stream and then feeding the gas stream into a particle/radiation interaction chamber for experimental evaluation. The radiative properties of the particle cloud were measured at 532 and 1064 nm, at optical thickness varying from 0.18 to 1.23. The scattered radiation was measured at angles ranging from 8.5° to 165° . The extinction and scattering coefficients and the scattering phase function were derived from the experimental measurements.

2.1 Particle Cloud Generation. The methodology for selecting the most suitable carbon black powder for the generation of a stable particle cloud is described in [10]. The particle dispersal system used to generate the particle cloud is shown in Fig. 1. It consisted of a flow regulator, a dispersion bowl containing the carbon black powder, a manifold attached to the bottom of the bowl and a particle/gas ejection nozzle. The carbon powder was kiln dried at 180°C for 8 hours before being loaded into the dispersion bowl. A pressurized nitrogen carrier gas was fed into the manifold and injected into the dispersion bowl through three radial orifices, fluidizing the powder. The gas/particle mixture was drawn out of the dispersion bowl via an axial center tube. Regulating the pressure of the carrier gas controlled the entrainment rate of the powder and therefore the mass loading of the mixture at the exit. The particle/gas mixture was then piped to a 30-liter glass vessel acting as a mixing chamber, where a secondary pure nitrogen stream was used to further dilute the mixture and fine-tune the optical thickness of the particle cloud. After initial settling and dilution in the mixing chamber, the particle cloud was fed into a secondary 30-liter glass vessel acting as final settling chamber for large particle agglomerates. The final mixture exited the settling chamber through a top valve, and entered the test chamber via a top manifold with six radial ports. The outlet from the test chamber was through a center outlet valve, integrally mounted on a filter holder used for gravimetric analysis. The particle generation system was operated until the desired optical thickness of the particle cloud in the test chamber was reached. The flow was then stopped and the outlet of the test chamber closed. The particle cloud usually stabilized after about half of an hour. The rate of particle settling in the test chamber was sufficiently slow to enable measurements at a practical steady state.

Repeatability of the experiments was confirmed by performing the same test at different times with different batches of the

same carbon black powder. The variation of the data was generally within the calculated error (95% confidence) of each measurement.

2.2 Particle Size Distribution. In situ samples of the particle cloud were taken for Scanning Electron Microscope (SEM) analysis. The cloud was probed at ages of 50 and 140 minutes at extinction coefficients of 1.55 and 0.62 m^{-1} respectively. The sampling probe consisted of a 10 cc syringe with a 150 mm long needle and an internal stage, where a SEM sample stub with a 12 mm diameter circular gold coated glass-plate was mounted. The probe containing the extracted cloud sample was placed in a vertical position for a minimum of 48 hours, allowing all the particles to settle on the sampling glass surface—thus representing the upper limit of the cloud's agglomerated state. Each sampling surface containing the settled particles was scanned at six random locations, far from the edges of the sampling disk in order to minimize the syringe's wall effect on the settled population distribution. At a given location the sample was scanned at magnifications of 10,000, 2000 and 500. The produced micrographs were digitally analyzed for particle counts, particle shape and size distribution. Individual single particles were also scanned at magnifications up to 30,000 for detailed examination of their shape and structure;

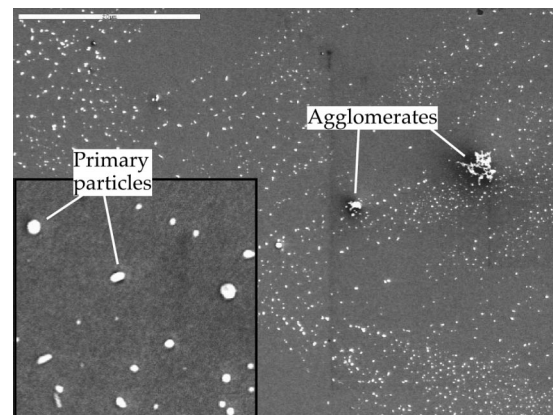


Fig. 2 SEM micrograph of a two-hour old Carbon particle cloud at magnification 2000. $\beta=0.62\text{ m}^{-1}$ at 1064 nm. Inset shows magnification of 10,000.

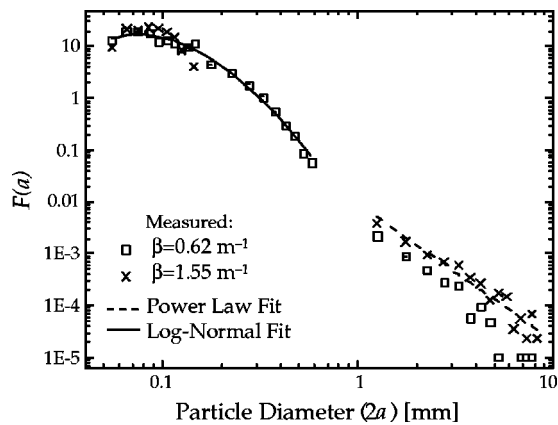


Fig. 3 Normalized particle population distribution of two particle clouds, $\beta=1.55 \text{ m}^{-1}$ and $\beta=0.62 \text{ m}^{-1}$ at 1064 nm. The distribution is a composite of scans at magnifications of 10,000, 2000 and 500.

however these scans were not included in the determination of the population distribution due to the scan's limited field of view.

Figure 2 shows a micrograph of a particle cloud sample at a magnification of 2000. It is seen that the particles are mainly single primary particles with a near spherical shape. Due to the small field of view, only a few agglomerates appear in the image. A lesser magnification of 500 was used to evaluate the size distribution of agglomerates. In all over 10,000 particles were counted.

The results of the digital image analysis, based on micrographs at magnifications of 10,000, 2000 and 500, were used to define the population distribution shown in Fig. 3. The distribution can be divided into two distinct populations: (i) primary particles with diameters ranging from 45 nm to 570 nm, having a time independent population distribution, and constituting 99.7% of all the counted particles. (ii) A small numerical fraction of large agglomerates, subjected to a time dependent settling process. The numerical amount of agglomerates was reduced by 50% within a time period of 90 min, indicating that there is settling but no spontaneous agglomeration of the particle cloud.

The shapes of the agglomerates were quite complex and far from spherical, and a few agglomerates had linear sizes up to 13

μm . The equivalent diameter of the agglomerates was defined as the diameter of a circle with the same cross sectional area as the projected area of the particle. The equivalent diameters of the agglomerates were in the range of 1.2–7.25 μm .

The size distribution in the primary particles range can be fitted to a normalized log-normal distribution function, as shown in Eq. (1):

$$F(a) = \frac{\delta_F}{(a - a_{\min}) \cdot \sqrt{\pi}} \cdot e^{-\delta_F^2 \cdot \{\ln[(a - a_{\min}) / a_{\text{median}} a_{\min}]\}^2} \quad (1)$$

The distribution of the agglomerates can be approximated as a power law, appearing as a straight line in Fig. 3. The two ranges appear to be disjoint, with no particles present in the size range of 0.6–1 μm .

The particle cloud's overall mass loading was determined by gravimetric analysis. The particle/gas mixture was pumped through a 0.1 μm cellulose membrane filter, which retained the particles on its surface. The filter holder was mounted on the top of the chamber, with a tube extending to the position of the measurement control volume. A flow meter/controller regulated the rate and amount of gas through the filter. The difference in weight of the filter before and after the test indicated the total mass of the particles in the mixture that was pumped through the filter. In order to verify that all the particles were retained on the 0.1 μm filter, a secondary filter with a mesh of 0.05 μm was placed behind the primary filter. The weight of the secondary filter was the same before and after the test, indicating that the primary filter retained practically all the particles.

2.3 Optical Properties Measurement. Transmission and scattering of radiation by the particle cloud were measured in a nephelometer that was especially constructed for this experiment, as shown in Fig. 4. The test chamber consisted of a 16-liter cylindrical stainless steel vessel with a diameter of 0.3 m. The chamber's inner surface was coated with a black adhesive layer, having an absorptivity of 95% in the visible and near IR. The lid of the test chamber had six radial injection ports and a central suction port with a filter holder for the gravimetric analysis.

Incident radiation was provided by two continuous-wave diode-pumped lasers at 532 nm and a 1064 nm with maximum power output of 103 mW and 75 mW, respectively. A polarizing prism mounted in front of the laser's exist aperture provided a beam polarized either parallel or perpendicular to the scattering plane.

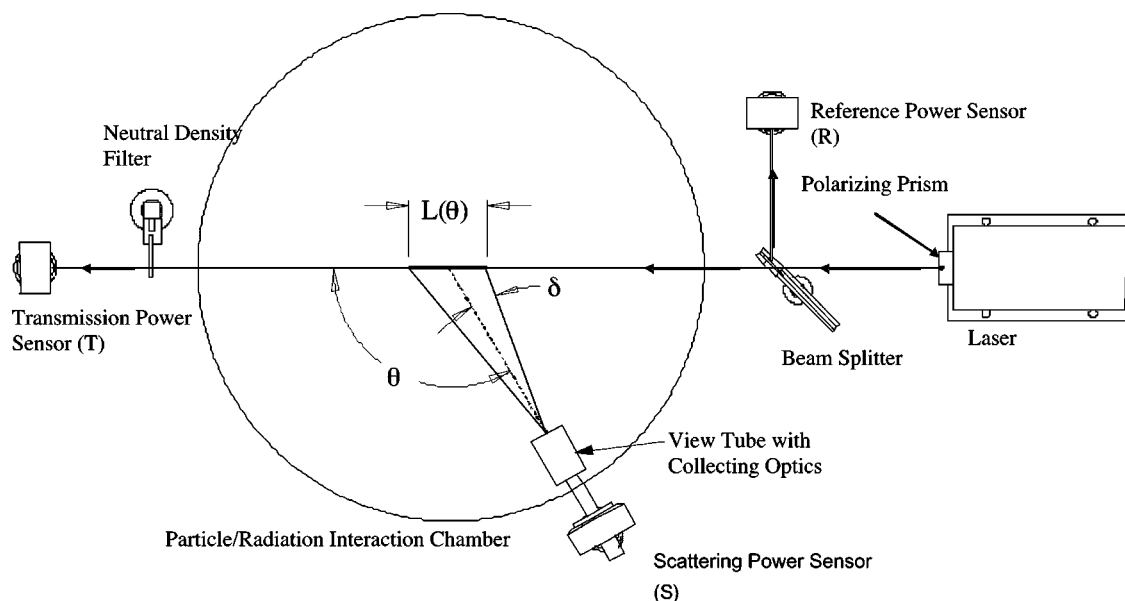


Fig. 4 Experimental apparatus for measurement of optical properties

The incident laser beam was split, with the secondary beam directed to a reference photodiode sensor mounted perpendicular to the path of propagation, marked *R* in Fig. 4. The readings of the reference sensor were used to compensate for laser output fluctuations.

The extinction of the incident beam by the particle cloud in the test chamber was measured by a silicone photodiode, marked *T* in Fig. 4, located aft of the exit aperture. A neutral density filter with a transmissivity of 32% was used to attenuate the beam strength to within the measurable range of the extinction sensor. Scattered radiation was measured at angles from 8.5° to 165° (limited by mechanical constraints of the apparatus) by a silicon photodiode, marked *S* in Fig. 4, installed on a rotating stage. The scattering was measured every degree up to $\theta=15^\circ$, and for the remaining angles-every five degrees. A view tube fixed to the photodiode sensor penetrated the wall of the test chamber through a semi circumferential slot. Sealing of the slot was achieved by a precision injection molded zipper, providing a moving aperture at the location where the view tube penetrated the chamber wall while sealing the rest of the slot. The collecting optics in the view tube consisted of a plano-convex lens with a focal length of 36 mm at the aperture and a tubular light stop. The lens was protected from particle contamination by a rotary solenoid operated guard, and was exposed only when data was acquired. The unit plane of the lens was located at a distance of 117 mm from the viewed control volume. The optics provided a half field of view angle of 1.1°, corresponding to a control-volume of length 4.5 mm at an angular position of 90°. The control volume length changed in inverse proportion to the sine of the scattering angle. At the limiting forward angle of 8.5° the length of the control volume was 30 mm, or 10% of the vessel's diameter. A correction for the angular dependence of the effective length of the viewed control volume was applied in the analysis of the measured data. The measured scattered energy was sampled at each location for 10 seconds, at a sampling rate of 100 Hz.

The measured data from all the sensors was gathered continuously by a 16-bit data acquisition system and recorded on a PC. Measurements commenced about 30 minutes after particle generation shut down, to permit the particle cloud in the test chamber to stabilize. A typical measurement sweep of all scattered directions lasted about 12 minutes, during which the particle cloud's optical thickness was essentially constant. Measurement sets were repeatedly taken at intervals of 30–45 minutes for about two hours.

2.4 Data Reduction. The baseline ratio of the measured reference power to the actual power entering the test chamber was established before each test by measuring the power entering the chamber without particles. A measurement sweep without particles was performed to determine the transmission at zero extinction, P_0 , and the setup-dependent background radiation. This measured bias error was later subtracted from the scattering measurements. The volumetric extinction coefficient of the particle cloud was calculated from the measurement of transmitted power at sensor *T*. The particle cloud was assumed to be spatially uniform in the plane of the laser beam, and the power in the forward direction due to forward scattering was assumed to be much lower than the transmitted power of the laser beam itself. The linear extinction coefficient is then given by:

$$\beta = \frac{1}{2R} \ln(P_0/P_T) \quad (2)$$

Sensor *S* (see Fig. 4) viewed a variable scattering volume, whose length L is a function of the scattering angle θ , and the lens half field of view δ . Since $\delta \ll 1$, this is approximately:

$$L(\theta) = \frac{2R\delta}{\sin \theta} \quad (3)$$

The measured scattered power at all scattering angles θ was normalized to geometry of scattering angle $\theta=90^\circ$ by multiplying

the measured local value by $\sin \theta$, to compensate for the variations in the length of the scattering volume. A second correction is to account for extinction over a distance of R between the scattering volume and the sensor, but this extinction is the same for all angles. The scattering phase function was derived from the power measured at the sensor by:

$$\Phi(\theta) = \frac{P_S(\theta) \cdot \sin \theta}{\frac{1}{2} \int_0^\pi P_S(\theta) \cdot \sin^2 \theta d\theta} \quad (4)$$

Since the medium consists of randomly oriented particles, the phase function depends only on the polar angle θ , and the total amount of scattered (outgoing) intensity is expressed by energy conservation of the phase function:

$$\int_0^\pi \Phi(\theta) \cdot \sin \theta d\theta = 2 \quad (5)$$

Equation (4) is then the ratio of the intensity intercepted at angle θ , normalized to the correct volume length, to the average (isotropic) scattered intensity.

The scattering measurements were repeated for incident radiation polarized parallel and perpendicular to the measurement plane. The total scattered power corresponding to an unpolarized source is found by averaging the parallel and perpendicular scattered power at an equal linear extinction coefficient and incident power.

Equation (4) takes into account the variable length of the beam that is visible from the sensor according to the polar angle θ . The total power scattered from a control volume of fixed length $L = 2R\delta$, corresponding to the section that is viewed by the sensor when it is positioned at $\theta=90^\circ$, is:

$$P_{sca} = \frac{2\pi R^2}{A_S} e^{\beta R} \int_0^\pi P_S(\theta) \cdot \sin^2 \theta d\theta \quad (6)$$

The integral in Eq. (6) requires values from the entire range of polar angle, while angular range of the measurement was between 8.5° and 165°. The ends of the range could not be measured due to mechanical limitations of the apparatus. This is a common problem in nephelometers, and some form of extrapolation is needed to provide the missing values. The procedure used here employed the intensity distributions calculated from Mie theory (Section 2.5). The calculated distribution was scaled to fit the first few measured points at angles above 8.5° to provide a smooth continuation. The same method was used to complete the phase function in the back scattering zone $165^\circ < \theta < 180^\circ$.

Based on Eq. (6) and the extinction coefficient from Eq. (2), we derive the linear scattering coefficient:

$$\sigma = \frac{P_{sca}}{P_0} \cdot \frac{e^{\beta R(1-\delta)}}{2R\delta} \quad (7)$$

2.5 Comparison to Mie Theory. The Mie theory provides a complete solution for the scattering of an incident planar wave by a particle, for the ideal case of a spherical and homogeneous particle [11]. We used the code BHMIE [15] to determine the extinction cross-section, the scattering cross section, and the scattered intensity field. These vary as a function of particle diameter (particles are assumed spherical) and incident radiation wavelength and polarization.

The complex index of refraction, which is difficult to measure directly, is a crucial input into the Mie theory calculation. We used the model of [16] which is supported by measurements in soot clouds [17–19]. The values of the complex index of refraction were calculated to 1.58–0.57*i* and 1.67–0.71*i* for wavelengths of 532 and 1064 nm, respectively.

The extinction cross-section, C_{ext} , of the particle cloud is related to the linear extinction coefficient β and to the particle number density N_p . Considering a polydisperse cloud with the popu-

Table 1 Absolute and relative uncertainty for the main measured and derived integral variables. The total uncertainty of σ and ω includes the contribution of the extrapolation of data to forward angles.

Parameter	Nominal Value	Total Uncertainty	Relative Uncertainty
β : Linear Extinction Coefficient, 532 nm (m^{-1})	0.946	0.026	2.8%
σ : Linear Scattering Coefficient, 532 nm (m^{-1})	0.346	+0.097–0.042	+28.0%–12.1%
σ : Linear Scattering Coefficient, 1064 nm (m^{-1})	0.373	+0.043–0.018	+11.5%–4.8%
ω : Single Scattering Albedo, 532 nm	0.366	+0.103–0.045	+28.1%–12.4%
ω : Single Scattering Albedo, 1064 nm	0.472	+0.056–0.026	+11.8%–5.6%
G : Particle Mass Loading (g m^{-3})	1.0	0.056	5.6%
K_e : Extinction Coefficient	8.25	1.61	19.5%

lation distribution function $F(a)$. The representative particle extinction cross section is a weighted average of the individual particles' extinction cross sections:

$$C_{ext} = \frac{\beta}{N_p} = \int_0^\infty C_{ext}(a) \cdot F(a) da \quad (8)$$

The cloud's scattering coefficient is derived from the individual particles' scattering cross sections using an expression analogous to Eq. (8).

The scattering phase function of a polydisperse cloud was also derived from the scattering properties of individual particles by averaging over the particle size distribution. The single-scattering phase function $\Phi(\Omega)$ is a function of only the polar angle θ for randomly oriented particles. It is related to the intensity field $I(\phi; a)$ created by scattering from an individual particle of radius a , as calculated by Mie theory, similar to Eq. (4):

$$\Phi(\theta) = \frac{2 \int_0^\infty I(\theta; a) F(a) da}{\int_{\theta=0}^\pi \int_{a=0}^\infty I(\theta; a) F(a) da \sin(\theta) d\theta} \quad (9)$$

The theoretical predictions of Eqs. (8) and (9) were computed in accordance with the measured particle size distribution, Fig. 3, of a 50 minutes aged cloud (full distribution). The computations were also repeated with the part of the distribution corresponding to the primary particles only (truncated distribution), as a comparison to assess the effect of the agglomerates.

2.6 Error Analysis. The uncertainty (95% confidence) of each measured parameter was determined by calculating its bias and precision errors due to the experimental apparatus and process unsteadiness [20]. When possible, the inherent bias errors of the sensors were measured and subtracted from the test results to reduce the uncertainty. For derived parameters, the error was computed from the errors of the independent variables [20]. The error analysis was performed for the measured data of representative tests with perpendicular and parallel polarization. The total uncertainty of the scattering coefficient and the scattering albedo includes the uncertainty of the extrapolated forward scattered energy for the scattering angles that could not be measured. Typical values for the measurement errors in the main variables are presented in Table 1.

For the scattering phase function, the uncertainty is a strong function of the scattering angle. At angles near 90° , the measured signal of the scattered energy was less than 1 nanowatt at single scattering conditions, which is close to the noise level of the photo diode sensor. Consequently, the uncertainty of the phase function for a thin cloud is high near $\theta \approx 90^\circ$, and much lower at other angles.

The extrapolation of the phase function to the forward and backward regions that were not directly measured also involves an amount of uncertainty. This was estimated by varying the scaling of the extrapolation function (Section 2.4) to find the lowest and

highest values where the function would still pass within the error bars of the measured points. These extreme scaling values were used in the normalization integral of the phase function, leading to the range of uncertainty for the scattering albedo.

The uncertainty of the values found in the literature for the complex index of refraction, used in the predictions based on Mie theory, is not known. The order of magnitude of the error can be estimated from the charts in [16], which present a comparison of the model to experimental values, but without discussion of experimental uncertainty, and without a quantitative measure of the discrepancies between the model and the experimental values. The charts show that most experimental points are within about 2% of the model, but some points are 10% or more away from the model prediction.

3 Results and Discussion

3.1 Extinction. Figure 5 shows the variation of the linear extinction coefficient at 532 nm with particle mass loading, measured by gravimetric analysis. The spread of the data is larger than the measurement error, probably since the different test series may have somewhat different particle size distributions. The slope of the extinction coefficient vs. mass loading curve is proportional to the dimensionless extinction coefficient K_e :

$$\beta = \frac{K_e}{\rho_p \cdot \lambda} \cdot G \quad (10)$$

The measured dimensionless extinction coefficient at 532 nm is compared with published data in Table 2. Agreement with [17,21,22] is good. The results of [19] are different, but the authors have already noted the discrepancy between their work and other published measurements.

The average measured extinction cross-section was found by combining the SEM particle counts with Eq. (8) for a cloud aged 140 minutes at a linear extinction of $\beta = 0.62 \text{ m}^{-1}$ at 1064 nm. The measured extinction cross-sections were in the range of $0.0125\text{--}0.0454 \mu\text{m}^2$, with an average value of $C_{ext} = 0.0276 \mu\text{m}^2$. While the individual samples were statistically too small and produced large scatter, the combined average of all samples provided a good match to the theoretical prediction of $C_{ext} = 0.0291 \mu\text{m}^2$. The particle number density, N_p , was determined by combining the measured specific extinction cross-

Table 2 Comparison of particle cloud extinction properties at about 532 nm

Particle type	Source	λ (nm)	G (g/m^3)	K_e
Carbon black	Current work	532	0.12–1.0	8.25 ± 1.61
Crude oil soot	Dobbins [17]	532 ^a	0.1	8.74
Acetylene soot	Wu [19]	515	7.1	5.1
Acetylene soot	Zhu [21]	633	–	8.1
Gaseous fuel soot	Krishnan [22]	515	–	7.9

^aInterpolated from published values.

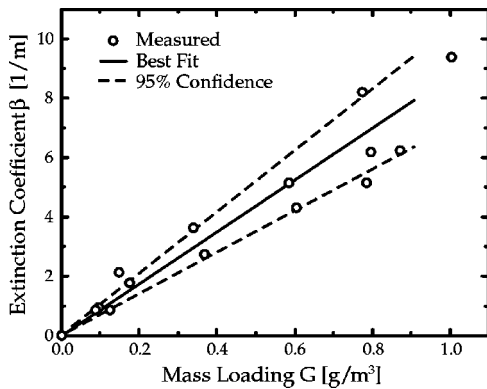


Fig. 5 Linear extinction coefficient vs. particle mass loading at $\lambda=532$ nm. The number density at a mass loading of 1 g/m^3 is $1.5 \cdot 10^{14}$ particles, and $K_e=8.25$

section, the slope of the data in Fig. 5, with Mie theory. At a mass loading of 1 g/m^3 , N_p was found to be $1.5 \cdot 10^{14}$ particles/ m^3 .

3.2 Scattering Phase Function. The scattering phase function was derived from the measured scattered power according to Eq. (4), acquired at linear extinction coefficients ranging from 4.1 m^{-1} for a young cloud to 0.8 m^{-1} for an aged cloud. Conditions for single scattering [11] were met for extinction coefficients lower than 1.5 m^{-1} . The measured scattering phase function at 532 and 1064 nm for both parallel and perpendicular polarization are shown in Fig. 6 *a-d*. Included in Fig. 6 is the Mie prediction of the scattering phase function for both perpendicular and parallel polarized incident radiation at wavelengths of 532 and 1064

nm. It was computed using the measured full particle size distribution, as discussed in Section 2.5. The best correlation between measured and predicted data is achieved for the particle cloud having the highest linear extinction coefficient, with an overall better match to the measured data at 1064 nm. The difference between the two polarization cases is most visible near 90° . For parallel polarization the scattering phase function exhibits a minimum at mid meridian polar angles and then increases towards the backward hemisphere, while for the perpendicular polarization the phase function decreases essentially monotonously with the polar angle.

Significant relative differences between the measured data and the prediction from Mie theory can be observed around scattering angle of 90° . These differences could be related to the uncertainty in the values of the index of refraction, as outlined in Section 2.6. The prediction depends on the index of refraction, and it is possible that different values of the index within its range of uncertainty would result in a better match between the theory and experiment. However, the scattered radiation intensity in this range of angles is typically lower than the radiation intensity in the forward directions by 2–3 orders of magnitude. Therefore, this discrepancy does not have a significant effect on an overall energy balance.

A comparison to the data of [18] is shown in Figs. 6*a* and *b*. These tests used fully developed (agglomerated) soot from an acetylene/air flame measured at a wavelength of 514.5 nm, close to the 532 nm used in the current work. The correspondence to our test results is surprising, considering the very different state of agglomeration.

The phase function prediction was repeated with the full particle size distribution, and with the truncated distribution containing primary particles only (see Section 2.2). The two predicted scattering phase functions are compared to the measured results in

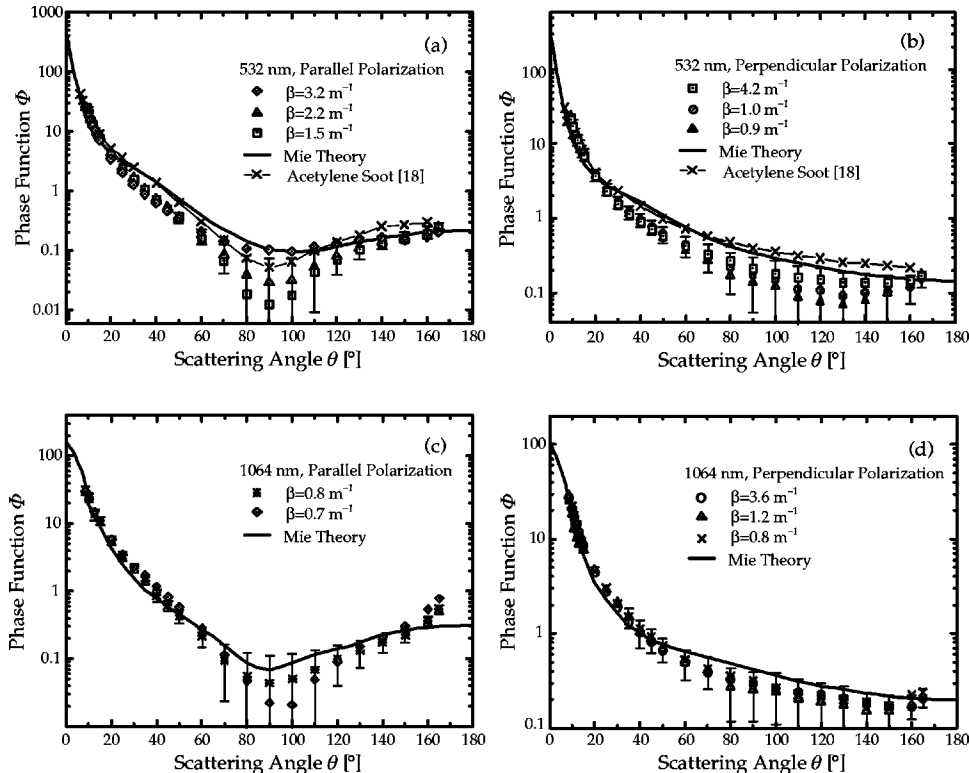


Fig. 6 Measured and predicted scattering phase function at 532 nm and 1064 nm. Mie theory results are based on the full particle population distribution, including agglomerates. Error bars represent 95% confidence. (a) 532 nm parallel polarization. (b) 532 nm perpendicular polarization. (c) 1064 nm parallel polarization. (d) 1064 nm perpendicular polarization.

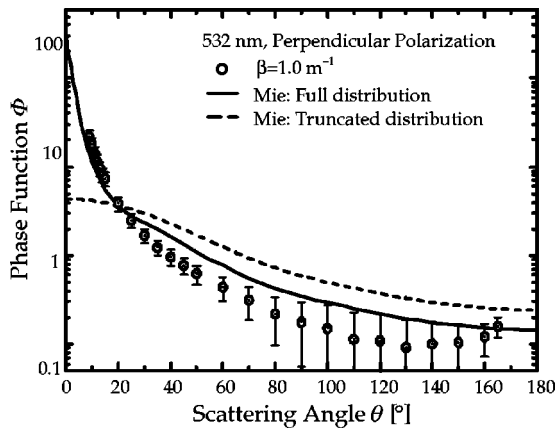


Fig. 7 Effect of the agglomerates on the scattering phase function for perpendicular polarization, $\beta=1.0 \text{ m}^{-1}$. The full particle population distribution includes agglomerates, and the truncated distribution includes primary particles only (diameter less than $1 \mu\text{m}$).

Fig. 7. Although the numerical fraction of the agglomerates is only 0.2%, they contribute 60% to the cloud's scattering cross section and exert a strong influence on the phase function. The presence of agglomerates changes the scattering characteristics of a particle cloud from a moderately asymmetrical to a strongly forward scattering pattern. The scattered energy in the forward direction of the particle cloud with agglomerates is two orders of magnitude higher than for a hypothetical cloud with primary particles only. A correct accounting of the particle size distribution is therefore crucial to the prediction of the scattering properties.

The forward scattered power within a lobe of 15° is about 62% at 532 nm and 48% at 1064 nm, while the back scattering in the aft 15° lobe is less than 0.4% of all the scattered power. Most of the forward scattered power is found at angles less than 9 degrees, where actual measurements were not possible and an extrapolation procedure was used, as explained in Section 2.4. The normalization of the phase function, and the fraction of the scattered power found in the forward direction, have therefore a relatively large uncertainty.

The spectral dependence of the scattering phase function is shown in Fig. 8 for perpendicular polarization at $\beta=0.90 \text{ m}^{-1}$. The dependence is weak in much of the angular range. A significant spectral effect can be seen only in the angular range of 80–150°. However, the values of the phase function in this range are about two orders of magnitude smaller than the values in the

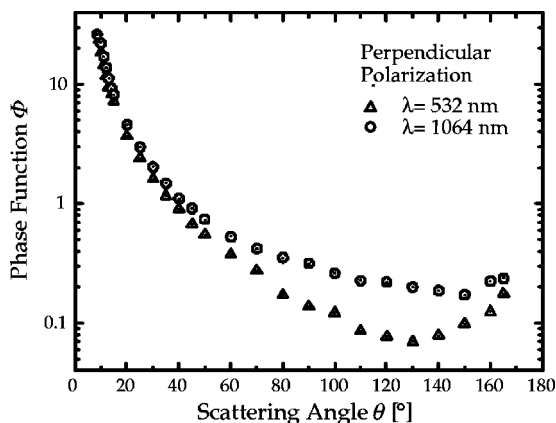


Fig. 8 Spectral dependence of phase function for perpendicular polarization at $\beta=0.90 \text{ m}^{-1}$.

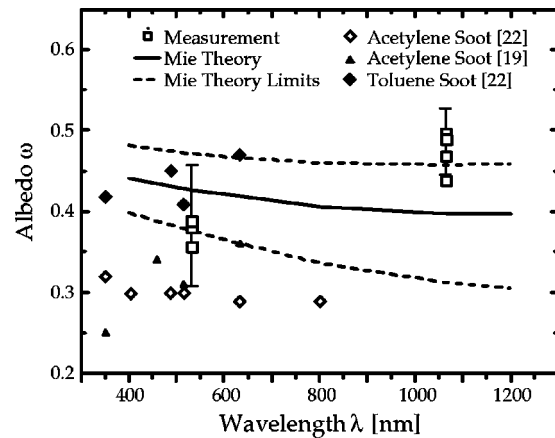


Fig. 9 Spectral dependence of the scattering albedo at single scattering conditions. Error bars represent 95% confidence. Data for acetylene is from [19,22]. Data for toluene is from [22].

forward direction. Therefore, the fraction of the scattered energy that is affected by this spectral difference is negligible.

3.3 Single Scattering Albedo. The linear extinction and scattering coefficients were evaluated from the measurements following Eqs. (2) and (7), respectively. The resulting single scattering albedo is shown in Fig. 9. The corresponding theoretical prediction was obtained according to Eq. (8) using the full particle size distribution.

The calculated fraction of the scattered energy in the forward lobe $\theta < 9^\circ$, which was not measured and was found by extrapolation (Section 2.5), is 46% at 532 nm and 29% at 1064 nm. The uncertainty of this extrapolation is the main cause for the large uncertainty of the measured albedo, especially at the shorter wavelength, as shown in Fig. 9. Uncertainty levels of 20% were reported by [22], which is similar to the error levels of this work at 532 nm.

The measured particle cloud scattering albedo increases with wavelength, from about 0.35 at 532 nm to about 0.45 at 1064 nm. The prediction using the full distribution does not capture the trend of the spectral variation of the scattering albedo. The experimental results do fall, however, within a deviation of 7% from the Mie theory prediction.

Figure 9 includes the upper and lower limits of the Mie prediction, due to uncertainties in the measured population distribution. It is seen that part of the measured albedo experimental error range falls within the theoretical prediction band. The uncertainty of the prediction due to the index of refraction would broaden this band of uncertainty even further. Considering the large uncertainties of both the measured and predicted results, the comparison of the albedo measured spectral behavior to the predicted is inconclusive.

Other measurements of the scattering albedo of fully agglomerated soot clouds [19], [22] are shown in Fig. 9. The albedo measured by [19] was in the range of 0.24–0.32 and showed only a weak spectral dependence. Later work [22] reported an even wider range of scattering albedo: from 0.19 to 0.47. The results for Acetylene and Toluene in [22] seem consistent with the findings of this work, with a similar spectral variation of increasing albedo with wavelength. Both of these reports use extrapolation of the scattered intensity to the forward region, but do not report the amount of uncertainty attributed to the scattering albedo due to this extrapolation. The lack of uncertainty information, and the wide dispersion of the reported data, prevent a conclusive comparison to [19] and [22].

Some of the experiments presented in [19] and [22] were performed at optical thickness that does not satisfy the requirement for single scattering. The measurements of scattered radiation

could therefore have been affected by secondary interactions. The measurements of this work, as shown in Fig. 9, were all performed at extinction coefficients of approximately $\beta = 1 \text{ m}^{-1}$, which satisfies the requirement for single scattering.

4 Conclusions

A stable polydisperse particle cloud has been successfully and repeatedly created by dispersing commercially available carbon black powder in an inert gas. The particle cloud stabilized during 20–30 minutes after being fed into a particle/radiation interaction chamber, and then changed very slowly for several hours. There was no indication of spontaneous particle agglomeration in the cloud. Two distinct populations could be discerned in the particle size distribution of the stabilized cloud. Primary particles constituted 99.7% of the particle count, with diameters ranging from 45 to 570 nm. Large agglomerates, with equivalent diameters ranging from 1.2 to 7.25 μm , provided 0.3% of the total particle count. The size distribution of the primary particles was well approximated by a log-normal function.

The optical properties of the particle cloud were investigated at wavelengths of 532 and 1064 nm. The non-dimensional extinction coefficient was evaluated as 8.25, consistent with previously published experimental data for other types of carbon particle clouds. The extinction cross section of the cloud was measured to 0.0276 μm^2 , which is close to the theoretical prediction of 0.0291 μm^2 .

The scattering behavior of the particle cloud was characterized by strong forward scattering. At 532 nm, 62% of the scattered energy was within a forward lobe of 15° , while the back scattering in the aft 15° lobe was less than 0.4%. At 1064 nm 48% of all scattered energy was in the forward 15° lobe. This characteristic is favorable for a solar particle receiver since it reduces energy losses by back scattering. For analysis of the radiative transfer and energy balance in the cloud using the Radiative Transfer Equation, the asymmetry of the phase function must be accounted for by using an appropriate anisotropic scattering model.

The measured scattering phase function was compared to the theoretically predicted data, based on Mie theory combined with the weighed contribution from each particle size, and to the experimental data published in [18]. The correlation between the measured and the predicted data was generally good, with the exception of parallel polarization at 532 nm where Mie theory over predicted the scattered energy for $30^\circ < \theta < 120^\circ$. The scattering phase function of the particle cloud showed only weak spectral dependence within the measurement range.

The scattering albedo was evaluated as 0.35 at 532 nm and 0.47 at 1064 nm. The experimental results showed an increase in albedo with wavelength, consistent with results of [22]. The corresponding prediction based on Mie theory showed the opposite trend of slow decrease with wavelength, similar to the results of [19]. An analysis of error in the albedo showed large uncertainty that originates in the extrapolation of the phase function to the forward angle range, which is not measured directly. This range accounts for a large fraction of the scattered energy.

The presence of a small amount of agglomerates can significantly change the particle cloud's scattering pattern. An agglomerate fraction of 0.3% in the particle count contributed 60% of the scattering cross section and significantly affected the phase function and the scattering albedo. This emphasizes the need to have a detailed knowledge of the particle size distribution of the investigated particle cloud. Using a well-defined commercial carbon powder, rather than soot particles that are generated in-situ, can provide a more consistent particle size distribution and is more suitable for robust operation of a solar receiver.

Using the classical Mie scattering theory, supplemented with detailed knowledge of the particle size distribution, we were able to predict the main features of the optical properties of a particle cloud containing a small fractional amount of agglomerates. The theory did not match the experiment in the scattering distribution near 90° . The scattered intensity in this range is very low, and

therefore the discrepancy is of little significance for the performance of the particle cloud within a solar receiver. The scattering albedo was also not well reproduced, since the uncertainty is large due to extrapolation to the forward angles. Past reported discrepancies between Mie theory and experimental data [13,14] might be attributed to the lack of detail in accounting for the particle population distribution.

Acknowledgments

Support for this work was provided by the Israel Ministry of National Infrastructure. The authors would like to thank Cabot Corporation Special Blacks Division (Massachusetts, USA), Columbian Chemicals Company (Georgia, USA), and Asbury Graphite Mills Inc. (New Jersey, USA) for providing carbon black powder for evaluation, and YKK-Zipper (New York, USA)/Star Zipper (Israel) for their assistance in sealing of the test chamber. We would also like to thank Prof. J. Katz and Prof. A. Yogevev for their valuable input.

Nomenclature

a	= Particle radius (m)
A	= Area (m^2)
C	= Cross section (m^2)
F	= Particle size distribution function
G	= Particle mass loading (kg m^{-3})
K_e	= Dimensionless extinction coefficient
L	= Length of beam section visible from the sensor (m)
N_p	= Particle number density (m^{-3})
P	= Power (W)
R	= Test chamber radius (m)
U	= Uncertainty

Greek

β	= Extinction coefficient (m^{-1})
δ	= Half field of view angle for the lens of sensor S (rad)
δ_F	= Population Distribution Factor
Φ	= Scattering phase function
λ	= Wavelength (m)
ρ_p	= Particle density (kg m^{-3})
σ	= scattering coefficient (m^{-1})
θ	= Polar angle (rad)
ω	= Albedo
Ω	= Solid angle (sr)

Subscripts

R, S, T	= Measurements of sensors R, S and T
0	= No particles

References

- [1] Abdelrahman, P., Fumeaux, Initial, and Suter, P., 1979, "Study of Solid-Gas Suspension used for Direct Absorption of Concentrated Solar Radiation," *Sol. Energy*, **22**, pp. 45–48.
- [2] Hunt, A. J., 1979, "A New Solar Receiver Utilizing a Small Particle Heat Exchanger," *4 Int. Soc. Energy Conversion Engrg. Conf.*, **1**, pp. 159–163.
- [3] Hunt, A. J., and Brown, C. T., 1983, "Solar Test Results of an Advanced Direct Absorption High Temperature Gas Receiver (SPHER)," *8 Solar World Congress*, Szokolay, S. V., Ed., Pergamon, **2**, pp. 959–963.
- [4] Bertocchi, R., Karni, J., and Kribus, A., In Press, "Experimental Evaluation of a Non-Isothermal High Temperature Solar Particle Receiver," *Energy—The International Journal*.
- [5] Steinfeld, A., 1998, "Research and Development of the Process Technology for Converting Concentrated Solar Energy into Chemical Fuels," PSI Report PSI-EF-REN(92)033.
- [6] Haueter, P., Moeller, S., Palumbo, R., and Steinfeld, A., 1999, "The Production of Zinc by Thermal Dissociation of Zinc Oxide-Solar Chemical Reactor Design," *Sol. Energy*, **67**, pp. 161–167.
- [7] Faeth, G. M., and Köylü, Ü. Ö., 1995, "Soot Morphology and Optical Properties in Nopremixed Turbulent Flame Environments," *Combust. Sci. Technol.*, **108**, pp. 207–229.
- [8] Erlick, C., Russel, L. M., and Ramaswamy, V., 2000, "A Microphysics-based Investigation of the Radiative Effects of Aerosol-cloud Interactions for Two MAST Experiment Case Studies," *J. Geophys. Res.*
- [9] Kaneyasu, N., and Murayama, S., 2000, "High Concentrations of Black Car-

- bon Over Middle Latitudes in the North Pacific Ocean," J. Geophys. Res., **105**, pp. 19881–19890.
- [10] Bertocchi, R., 2002, "Carbon Particle Cloud Generation for a Solar Particle Receiver," J. Sol. Energy Eng., **124**, pp. 230–236.
- [11] van de Hulst, H. C., 1957, *Light Scattering by Small Particles*, Wiley, New York.
- [12] Kocifaj, M., and Lukac, J., 1998, "Using the Multiple Scattering Theory for Calculation of the Radiation Fluxes from Experimental Aerosol Data," J. Quant. Spectrosc. Radiat. Transf., **60**, pp. 933–942.
- [13] Erickson, W. D., Williams, G. C., and Hottel, H. C., 1964, "Light Scattering Measurements on Soot in a Benzene-Air Flame," Combust. Flame, **8**, pp. 127–132.
- [14] Dalzell, W. H., Williams, G. C., and Hottel, H. C., 1970, "A Light Scattering Method for Soot Concentration Measurements," Combust. Flame, **14**, pp. 161–170.
- [15] Bohren, C. F., and Huffman, D. K., 1983, *Absorption and Scattering of Light by Small Particles*, Wiley, New York.
- [16] Dalzell, W. H., and Sarofim, A. F., 1969, "Optical Constant of Soot and their Application to Heat Flux Calculations," J. Heat Transfer, **91**, pp. 100–104.
- [17] Dobbins, R. A., Mulholland, G. W., and Bryner, N. P., 1994, "Comparison of a Fractal Smoke Optics Model with Light Extinction Measurements," Atmos. Environ., **28**, pp. 889–897.
- [18] Köylü, Ü. Ö., and Faeth, G. M., 1994, "Optical Properties of Overfires Soot in Buoyant Turbulent Diffusion Flames at Long Residence Times," J. Heat Transfer, **116**, pp. 152–159.
- [19] Wu, J. S., Krishnan, S. S., and Faeth, G. M., 1997, "Refractive Indices at Visible Wavelengths of Soot Emitted from Buoyant Turbulent Flames," J. Heat Transfer, **119**, pp. 230–237.
- [20] Taylor, J. R., 1982, *An Introduction to Error Analysis*, University Science Books.
- [21] Zhu, J., Choi, M. Y., Mulholland, G. W., and Gritzo, L. A., 2000, "Measurements of Soot Optical Properties in the Near Infrared Spectrum," Int. J. Heat Mass Transfer, **43**, pp. 3299–3303.
- [22] Krishnan, S. S., Lin, K. C., and Faeth, G. M., 2000, "Extinction and Scattering of Soot Emitted from Turbulent Diffusion Flames for Wavelengths of 250–5200 nm," *34th National Heat Transfer Conference*, S. C. Yao, Ed., Pittsburgh, ASME.